Electrical magnetochiral anisotropy in trigonal tellurium from first principles

Xiaoxiong Liu, 1, 2, 3, 4, 5 Ivo Souza, 6, 7 and Stepan S. Tsirkin 6, 7

¹ Physik-Institut, Universität Zürich, Winterthurerstrasse 190, CH-8057 Zürich, Switzerland
 ² Shenzhen Institute for Quantum Science and Engineering and Department of Physics,
 Southern University of Science and Technology (SUSTech), Shenzhen 518055, China
 ³ Quantum Science Center of Guangdong-Hong Kong-Macao Greater Bay Area (Guangdong), Shenzhen 518045, China
 ⁴ Shenzhen Key Laboratory of Quantum Science and Engineering, Shenzhen 518055, China
 ⁵ International Quantum Academy, Shenzhen 518048, China
 ⁶ Centro de Física de Materiales, Universidad del País Vasco, 20018 San Sebastián, Spain
 ⁷ Ikerbasque Foundation, 48013 Bilbao, Spain
 (Dated: October 10, 2024)

Structural chirality gives rise to characteristic responses that change sign with the handedness of the crystal structure. One example is electrical magnetochiral anisotropy (eMChA), a change in resistivity that depends linearly on the applied current and on the magnetic field. Motivated by recent measurements of a strong eMChA in p-doped trigonal tellurium, we carry out an ab initio study of the eMChA response in this material as a function of temperature and doping concentration. We use the semiclassical Boltzmann transport formalism within the constant relaxation-time approximation to express the bulk eMChA response tensor in terms of the energy dispersion, intrinsic magnetic moment, and Berry curvature of the conduction Bloch states. We find that the orbital Zeeman coupling dominates the calculated response, with smaller contributions coming from the spin Zeeman coupling and from the Berry curvature, and that the effect is maximal when both the current and magnetic field are along the trigonal axis. The calculated data shows a reasonable agreement with the experiments. We provide the open-source code to facilitate further ab initio studies of eMChA in other materials.

Introduction. The electrical transport properties of nonmagnetic crystals change under an applied magnetic field, leading to different phenomena that can be generally described as an expansion of the current in powers of the electric and magnetic fields \boldsymbol{E} and \boldsymbol{B} ,

$$j_a = \sigma_{ab}(\mathbf{B})E_b + \sigma_{abc}(\mathbf{B})E_bE_c + \dots$$
 (1)

The ordinary and planar Hall effects [1], as well as the ordinary magnetoresistance [2], are all contained in the first term. Electrical responses that are quadratic in \boldsymbol{E} (second term) become allowed in noncentrosymmetric media, and have recently attracted a great deal of attention. One example is the nonlinear anomalous Hall effect, a transverse response that occurs in the absence of an external magnetic field and without requiring magnetic order [3–5].

Another example of an E^2 response is electrical magnetochiral anisotropy (eMChA) [6, 7], an anomalous magnetoresistance that is bilinear in B and in the applied current I. The resistance of a material exhibiting eMChA takes the form

$$R(B, I) = (1 + \beta B^2 + \gamma IB)R_0,$$
 (2)

where the coefficients β and γ describe ordinary magnetoresistance and eMChA, respectively (the tensorial character of the various quantities is ignored for now). The coefficient γ vanishes in centrosymmetric systems, and in chiral media it is equal in magnitude and opposite in sign for right- and left-handed enantiomers. As eMChA is not restricted to chiral systems, it is sometimes referred

to by other names such as bulk current-rectification effect [8], nonreciprocal resistance [8, 9], and unidirectional magnetoresistance [10, 11].

The eMChA has been measured in several chiral systems including bismuth helices [6], single-walled carbon nanotubes [12], molecular conductors [13], noncentrosymmetric transition metal dichalcogenide [14], and trigonal tellurium [11, 15–17], as well as in the nonchiral polar semiconductor BiTeBr [8]. Similar nonreciprocal responses have also been reported both in Josephson junctions [18, 19] and in junction-free superconductors [20–22].

Recently, Calavalle et al. [11] reported the manipulation and detection of eMChA in tellurium nanowires at low temperatures. Motivated by this work and by that of Refs. [15, 16], here we undertake an ab initio study of the eMChA response in p-doped trigonal tellurium (p-Te). As it crystallizes in the simplest chiral structure with only three atoms per cell, elemental tellurium is an ideal prototype material for performing bulk ab initio calculations of eMChA.

Bulk tensorial description. To formulate eMChA as a bulk response, we divide Eq. (2) by the cross-section area A of the sample, converting from resistance R and current I to resistivity ρ and current density j. Dropping the ordinary magnetoresistance term and defining $\gamma' = \gamma A$, we obtain

$$\rho(B,j) = (1 + \gamma' j B) \rho_0, \qquad (3)$$

where the tensorial character is again ignored.

While experimentally one applies currents and mea-

sures voltages, microscopic theory deals instead with the current density induced by the applied fields, as in Eq. (1). We expand $\sigma(\mathbf{B})$ in powers of \mathbf{B} , leaving only terms that are proportional to E and E^2B to find

$$j_a = \sigma_{ab}E_b + \sigma_{abcd}E_bE_cB_d, \qquad (4)$$

where σ_{ab} is the linear Ohmic conductivity, σ_{abcd} is the eMChA magnetoconductivity, and a summation over repeated Cartesian indices is implied. Solving for E as a function of B and j to order Bj^2 , one arrives at the following tensorial generalization of Eq. (3),

$$\rho_{ae}(\mathbf{B}, \mathbf{j}) = (\delta_{ab} + \gamma'_{abcd} j_c B_d) \rho_{be}, \qquad (5)$$

where $\rho_{ac}\sigma_{cb} = \delta_{ab}$, and

$$\gamma'_{abcd} = -\rho_{aa'}\sigma_{a'bb'd}\rho_{b'c} \tag{6}$$

is the bulk eMChA tensor. Thus, the main task of a predictive bulk theory of eMChA is to evaluate the conductivity tensors σ_{ab} and σ_{abcd} defined by Eq. (4) that are needed to evaluate γ'_{abcd} from Eq. (6). Note that while σ_{abcd} has the intrinsic permutation symmetry $\sigma_{abcd} = \sigma_{acbd}$, the relation $\gamma'_{abcd} = \gamma'_{acbd}$ only holds when the Cartesian axes are chosen as principal axes of the Ohmic resistivity ρ_{ab} .

Boltzmann-transport theory of eMChA. To develop a microscopic theory of eMChA in nonmagnetic conductors, we resort to the semiclassical Boltzmann formalism with Berry-curvature and spin/orbital-moment corrections, which are widely used to describe linear and nonlinear (magneto)transport in solids [23, 24]. Within the constant relaxation time approximation adopted below, this formalism accounts for intrinsic band structure effects but leaves out extrinsic effects such as skew scattering and side jump.

In the Boltzmann formalism, the current density takes the form

$$\mathbf{j} = -\int [d\mathbf{k}] \, D\dot{\mathbf{r}} f \,, \tag{7}$$

where the integral is over the Brillouin zone, $[d\mathbf{k}] \equiv d^3k/(2\pi)^3$, $\dot{\mathbf{r}}$ is the electron velocity, f is the nonequilibrium distribution function, and $D \equiv 1 + \Omega_{\mathbf{k}} \cdot \mathbf{B}$, with $\Omega_{\mathbf{k}}$ the Bloch-state Berry curvature. We use units where $e = \hbar = m_e = 1$, and omit band summations.

We determine f by solving the Boltzmann transport equation in the constant relaxation-time approximation,

$$\dot{\mathbf{k}} \cdot \nabla_{\mathbf{k}} f = \frac{f_0(\tilde{\epsilon}_{\mathbf{k}}) - f}{\tau} \,, \tag{8}$$

where $f_0(\tilde{\epsilon}_{\mathbf{k}})$ is the equilibrium Fermi-Dirac distribution function evaluated at the Zeeman-shifted band energy $\tilde{\epsilon}_{\mathbf{k}} = \epsilon_{\mathbf{k}} - \mathbf{m}_{\mathbf{k}} \cdot \mathbf{B}$, with $\mathbf{m}_{\mathbf{k}}$ the total (spin plus orbital) magnetic moment $\mathbf{m}_{\mathbf{k}}$ of a Bloch state [25]. The velocities

 $\dot{\mathbf{r}}$ and $\dot{\mathbf{k}}$ in real space and in reciprocal space satisfy the coupled equations [23]

$$\dot{\mathbf{r}} = \nabla_{\mathbf{k}} \tilde{\epsilon}_{\mathbf{k}} - \dot{\mathbf{k}} \times \mathbf{\Omega}_{\mathbf{k}}, \tag{9a}$$

$$\dot{\mathbf{k}} = -\mathbf{E} - \dot{\mathbf{r}} \times \mathbf{B} \,, \tag{9b}$$

which can be decoupled as

$$D\dot{\mathbf{r}} = \nabla_{\mathbf{k}}\tilde{\epsilon}_{\mathbf{k}} + \boldsymbol{E} \times \boldsymbol{\Omega}_{\mathbf{k}} + (\nabla_{\mathbf{k}}\tilde{\epsilon}_{\mathbf{k}} \cdot \boldsymbol{\Omega}_{\mathbf{k}}) \boldsymbol{B}, \quad (10a)$$

$$-D\dot{\mathbf{k}} = \mathbf{E} + \nabla_{\mathbf{k}}\tilde{\epsilon}_{\mathbf{k}} \times \mathbf{B} + (\mathbf{E} \cdot \mathbf{B}) \Omega_{\mathbf{k}} . \tag{10b}$$

Next, we expand f in Eq. (8) as $f = \sum_{n=0}^{\infty} f_n \tau^n$ to obtain the recursive relation

$$f_{n+1} = -\tau \dot{\mathbf{k}} \cdot \nabla_{\mathbf{k}} f_n , \qquad (11)$$

which is solved starting from $f_0 = f_0(\tilde{\epsilon}_{\mathbf{k}})$ using Eq. (10b) for $\dot{\mathbf{k}}$. Finally, the current density is obtained as a power series in \mathbf{E} and \mathbf{B} by inserting the resulting expression for f into Eq. (7), together with Eq. (10a) for $\dot{\mathbf{r}}$.

At linear order in E, the above procedure yields the familiar result for the Ohmic conductivity,

$$\sigma_{ab} = \tau \int [d\mathbf{k}] \, v_a v_b f_0' \,, \tag{12}$$

where $f'_0 = df_0(\epsilon)/d\epsilon|_{\epsilon=\epsilon_{\mathbf{k}}}$. The derivation of the expression at order $\mathbf{E}^2\mathbf{B}$ for the eMChA conductivity σ_{abcd} is outlined in the Supplementary Material [26]. Here, it suffices to note that in nonmagnetic conductors the only nonvanishing contribution comes from f_2 , and so it is proportional to τ^2 . In particular, there is no contribution coming from the \mathbf{B} dependence of the chemical potential, which is an even function of \mathbf{B} in crystals with time-reversal symmetry [25]. The resulting expression

$$\sigma_{abcd} = \sigma_{abcd}^{Z} + \sigma_{abcd}^{\Omega} \tag{13}$$

comprises the Zeeman (Z) and Berry curvature (Ω) terms

$$\sigma_{abcd}^{\mathbf{Z}} = \tau^2 \int [d\mathbf{k}] \left(v_{abc} m_d - v_c \partial_{ab} m_d \right) f_0' \qquad (14)$$

and

$$\sigma_{abcd}^{\Omega} = -\tau^{2} \int [d\mathbf{k}] \left[2v_{ab}v_{c}\Omega_{d} + v_{a}v_{c}\partial_{b}\Omega_{d} - \delta_{cd}(2v_{ae}v_{b}\Omega_{e} - v_{a}v_{e}\partial_{b}\Omega_{e}) - \delta_{ad}(v_{be}v_{c}\Omega_{e} + v_{c}v_{e}\partial_{b}\Omega_{e}) - \varepsilon_{edf}\varepsilon_{abg}v_{f}\partial_{e}\Omega_{g}v_{c} \right] f'_{0},$$
(15)

where $\partial_a \equiv \partial/\partial_{k_a}$, $v_a \equiv \partial_a \epsilon_{\mathbf{k}}$ is the band velocity, $v_{ab} \equiv \partial_{ab} \epsilon_{\mathbf{k}}$ is the inverse effective-mass tensor, and $v_{abc} \equiv \partial_{abc} \epsilon_{\mathbf{k}}$. Note that only the part of σ_{abcd} that is invariant under permutations of indices b and c contributes to the physical effect, while in Eqs. (14) and (15) the symmetry under $b \leftrightarrow c$ is not explicitly seen. Therefore, we further use the combinations $(\sigma_{abcd} + \sigma_{acbd})/2$

for the component σ_{abcd} . The Zeeman response can be further separated into spin and orbital parts, yielding three types of contributions in total. The spin-Zeeman response requires spin-orbit coupling, while the orbital-Zeeman and Berry curvature responses are present even without spin-orbit coupling.

In the above derivation, we did not consider the corrections to the orbital moment and Berry curvature due to applied fields [24, 27]. Such corrections only affect lower-order terms E^1B^1 (Hall effect) and E^2B^0 (nonlinear Hall effect), which are purely transverse; therefore, the longitudinal resistivity remains unchanged. In this manuscript, we mainly focus on the longitudinal effect.

Equations (12-15) are the needed ingredients to evaluate the intrinsic contributions to the bulk eMChA tensor γ'_{abcd} in Eq. (6). Inversion symmetry implies $\epsilon(\mathbf{k}) = \epsilon(-\mathbf{k})$, $\mathbf{m}(\mathbf{k}) = \mathbf{m}(-\mathbf{k})$, and $\Omega_{\mathbf{k}}(\mathbf{k}) = \Omega_{\mathbf{k}}(-\mathbf{k})$; as a result, every term in Eqs. (14) and (15) vanishes in centrosymmetric crystals, yielding $\gamma'_{abcd} = 0$ as expected. Since σ_{ab} is linear in τ and σ_{abcd} is quadratic, γ'_{abcd} becomes independent of τ in the constant relaxation time approximation.

In the following, we first outline the computational methods, and then report and discuss the numerical results of our *ab initio* calculations for *p*-Te.

Computational methods. The unit cell of trigonal Te contains three atoms disposed along a spiral chain, with the chains arranged on a 2D hexagonal lattice. The fully-relativistic electronic structure of the pristine (undoped) right-handed crystal (space group P3₁21) is evaluated via density-functional theory (DFT) in the pseudopotential framework, using the HSE06 hybrid functional [28] implemented in the VASP code package [29–31].

In order to evaluate the needed k-space quantities accurately and efficiently, we employ the Wannier interpolation scheme [32]. The Wannier functions are constructed using the Wannier90 code package [33], starting from atom-centered s and p trial orbitals. In order to avoid artifacts due to possible numerical violations of crystal symmetries by the Wannier model, the Wannier Hamiltonian and orbital-based matrix elements are symmetrized so as to satisfy the point-group symmetries.

We have implemented all terms in Eqs. (14) and (15) in the WannierBerri code package [34]. Wannier interpolation allows us to evaluate band properties and their momentum-space derivatives directly, without finite difference schemes [35]. We perform the Brillouin-zone integrals on a symmetry-irreducible part of a regular grid of $300 \times 300 \times 300$ points, using 30 adaptive refinement iterations, and employing the tetrahedron method [36, 37] to accurately describe the Fermi occupation factors $-f'_0$.

Numerical results. The eMChA conductivity σ_{abcd} is a nonmagnetic polar tensor symmetric in bc, with the Jahn symbol eV[V²]V. Table I shows the constraints imposed on that tensor by the point group symmetry of trigonal tellurium.

TABLE I. Symmetry constraints on the components of the eMChA conductivity tensor σ_{abcd} in crystal class 32. The three largest calculated components in trigonal tellurium are highlighted in bold. The table was generated using the MTENSOR routine [38] provided by the Bilbao Crystallographic Server [39].

32		bc = cb					
σ_{abcd}		xx	yy	zz	yz	xz	xy
	xx	σ_{yyyy}	σ_{yxxy}	σ_{yzzy}	$-\sigma_{yyzy}$	0	0
	xy	0	0	0	0	$-\sigma_{yyzy}$	$(\sigma_{yyyy} - \sigma_{yxxy})/2$
	xz	0	0	0	0	σ_{yyzz}	$-\sigma_{yyyz}$
	yx	0	0	0	0	$-\sigma_{yyzy}$	$(\sigma_{yyyy} - \sigma_{yxxy})/2$
ad	yy	σ_{yxxy}	σ_{yyyy}	σ_{yzzy}	σ_{yyzy}	0	0
	yz	$-\sigma_{zyyy}$	σ_{yyyz}	0	σ_{yyzz}	0	0
	zx	0	0	0	0	σ_{zyzy}	$-\sigma_{zyyy}$
	zy	$-\sigma_{zyyy}$	σ_{zyyy}	0	σ_{zyzy}	0	0
	zz	σ_{zyyz}	σ_{zyyz}	σ_{zzzz}	0	0	0

In p-Te the Fermi energy cuts the top of the upper valence band shown in Fig. 1(a), forming a small hole-like Fermi pocket near the H point. We find that when the Fermi level is placed near the top of the upper valence band, the largest component of the eMChA tensor is

$$\gamma_{zzzz}' = -\rho_{zz}^2 \sigma_{zzzz} \tag{16}$$

and the second largest components are

$$\gamma'_{xzzx} = \gamma'_{yzzy} = -\rho_{yy}\rho_{zz}\sigma_{yzzy} \tag{17}$$

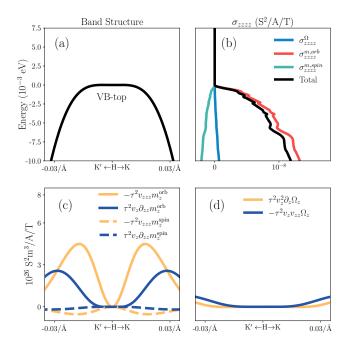
(here $\rho_{xx} = \rho_{yy}$), while other symmetry-allowed components are orders of magnitude smaller (details in Supplementary Material [26]). The predominance of components driven by magnetic field along the trigonal z axis suggests that the strong coupling to m_z is crucial to the effect. As discussed earlier, the intrinsic eMChA conductivity has three types of contributions: orbital Zeeman, spin Zeeman, and Berry curvature. For p-Te, the zzzz component is strongly dominated by orbital Zeeman contributions, as shown in Fig. 1(b). To understand this result, consider the zzzz components of Eqs. (14) and (15),

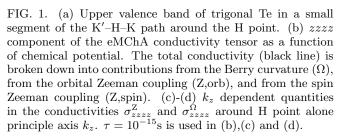
$$\sigma_{zzzz}^{Z} = \tau^{2} \int [d\mathbf{k}] \left(-v_{zzz}m_{z} + v_{z}\partial_{zz}m_{z} \right) \left(-f_{0}' \right), \quad (18)$$

$$\sigma_{zzzz}^{\Omega} = \tau^{2} \int [d\mathbf{k}] \left(v_{z}^{2}\partial_{z}\Omega_{z} - v_{z}v_{zz}\Omega_{z} \right)$$

$$- 3v_{zx}\Omega_{x}v_{z} - 3v_{zy}\Omega_{y}v_{z} \right) \left(-f_{0}' \right). \quad (19)$$

Due to the $-f'_0$ factors, only states located at the Fermi surface contribute to the response at zero temperature. Panels (c) and (d) of Fig. 1 show the evolution with k_z , near the H point, of each term in the integrand of Eqs. (18) and (19) (since Ω_x and Ω_y are negligible near H, we drop the terms in the second line of Eq. (19)).





In Fig. 1(c), the contribution from each term in Eq. (18) is further separated into orbital and spin parts; the orbital contributions are dominant, because $|m_z^{\rm orb}| \gg |m_z^{\rm spin}|$ in the upper valence band of Te [40]. In each channel (spin or orbital), the first term in Eq. (18) dominates over the second; this is due to the weak "camel-back" shape of the upper valence band near H, which suppresses the band gradient v_z but not the higher derivative v_{zzz} . That also explains why the Berry-curvature contributions in Fig. 1(d) are much smaller than the orbital-Zeeman ones in Fig. 1(c), as both terms in the first line of Eq. (19) contain v_z factors.

The temperature-dependent σ_{zz} , σ_{zzzz} and γ'_{zzzz} are shown in Fig. 2(a,b,c) respectively, which are calculated using the temperature-dependent Fermi-Dirac distribution function $f_0(T,\mu,\epsilon)$ at chemical potential μ . Fig. 2(d) displays σ_{zzzz} and σ_{zz} at four acceptor concentrations at 0K. As the hole acceptor concentration increases in p-Te, the Fermi level shifts downward, resulting in changes in σ_{zzzz} and σ_{zz} . The specific Fermi level for various acceptor concentrations is shown in Fig. 2(d).

When the Fermi level is close to the top of the valence band, the acceptor concentration is low, and the sensitivity of γ'_{zzzz} to temperature becomes significant com-

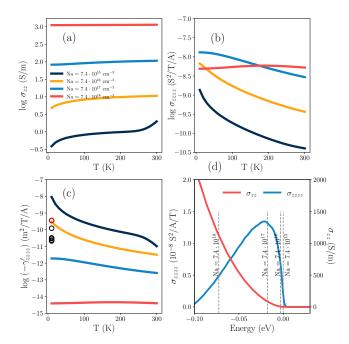


FIG. 2. Calculated temperature dependence, for different acceptor concentrations $N_{\rm a}$, of (c) Ohmic conductivity σ_{zz} , (b) eMChA conductivity σ_{zzzz} , and (c) eMChA parameter γ'_{zzzz} . $\tau = 10^{-15} {\rm s}$ is used in (a) and (b). The circles in panel (c) denote the values measured in six different samples in Ref. [11]; the red circle denotes the sample whose size was determined most precisely [11]. (d) σ_{zzzz} and σ_{zz} as functions of chemical potential at 10K. The gray dashed lines indicate the chemical potentials corresponding to four different acceptor concentrations.

pared to higher acceptor concentrations. In σ_{zzzz} , there is a high peak next to the energy gap, leading to extreme changes due to temperature because of the smearing of the peak. The fact that σ_{zzzz} and $1/\sigma_{zz}$ have slopes in a similar trend that exacerbates the sensitivity of γ'_{zzzz} to temperature when T < 50 K. When $N_{\rm a} = 7.4 \cdot 10^{18} {\rm cm}^{-3}$, the corresponding curve in Fig. 2(b) has an opposite slope because the chemical potential is on the other side of the peak of σ_{zzzz} (see Fig. 2(d)). In the temperature dependent γ' measurement in Ref.[16], $\gamma' \approx 10^{-12} {\rm m}^2/{\rm T/A}$ for gate voltage $V_g = 80{\rm V}$ at 20K. From 20K to 160K, γ' drops by one order of magnitude, see Fig. 4 and Fig. 2(a) therein. It matches our simulation when acceptor concentration is between $7.4 \cdot 10^{16} {\rm cm}^{-3}$ to $7.4 \cdot 10^{17} {\rm cm}^{-3}$.

In the experimental measurement of p-Te nanowires in Ref.[11], eMChA was scanned over all possible directions of the magnetic field, and it was confirmed that the response is largest when \boldsymbol{B} is parallel to the applied current, in agreement with our simulation. The eMChA resistivity was measured for six samples. However, to extract γ'_{zzzz} the exact dimensions of the nanowires are needed, which were determined only for one of them. Assuming that the size is the same (at least in order of magnitude) for all nanowires, the value of γ'_{zzzz} for six

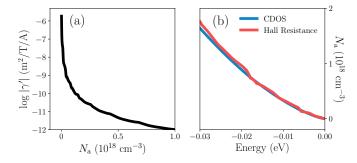


FIG. 3. (a) Calculated γ'_{zzzz} as a function of acceptor consentration. (b) Comparison between acceptor concentration calculated using precise cumulative density of states (CDOS) and Hall resistance measurement.

nanowires at 10K may be estimated within the range of $[10^{-11}, 10^{-9}]$ m²/T/A. The acceptor concentration was estimated as $7.4 \cdot 10^{17}$ cm⁻³ using Hall resistance $R_{\rm H}$,

$$N_{\rm a} = \frac{B_c}{ewR_{\rm H}} = \frac{\sigma_{aa}\sigma_{bb}}{e\sigma_{abc}^{H}} , \qquad (20)$$

where w is the thickness of a nanowire. It also can be evaluated from first principle by evaluating Ohmic and Hall conductivity $\sigma_{aa/bb}$ and σ_{abc}^{H} within the Boltzman transport theory [1]. Strictly speaking, the first equality in Eq. (20) is only valid for a parabolic band dispersion. Even though the valence band of Te near the H point is strongly non-parabolic, by means of accurate calculations we confirm that Eq. (20) is still valid close to the top of the valence band, and the error only increases slightly as the chemical potential moves away from the top of the valence band, see Fig. 3(b). As shown in Fig. 2(a), our estimated value of γ'_{zzzz} is significantly lower for this acceptor concentration. However, γ'_{zzzz} is extremely sensitive to acceptor concentration. A tiny change of N_a changes orders of magnitude of γ'_{zzzz} , see Fig. 3(a). Therefore, an excellent agreement with the experimental value is difficult to achieve.

In earlier measurements at room temperature [15], the largest component of the γ tensor was found to be in the range of $[10^{-9}, 10^{-8}]$ m²/T/A with an acceptor concentration of around $10^{16} {\rm cm}^{-3}$. However, it was observed that the effect is maximized when the magnetic field is perpendicular to the current. This contradicts the symmetry analysis in Table I, and therefore cannot be described as a bulk property of trigonal tellurium, regardless of the microscopic mechanism implied.

The sign of the effect. Within constant relaxation time approximation we find that for the right-handed crystal, the sign of the eMChA resistivity (the γ'_{zzzz} parameter) is negative, or equivalently, the sign of the eMChA resistivity is positive. The opposite signs are expected for the left-handed crystal. This is consistent with the experimental results in Ref.[11]. However, after publication of the preprint of the present manuscript, another arti-

cle appeared [41], that claims the opposite sign of the eMChA conductivity. The lack of information on the geometrical size of the samples in Ref.[41] does not allow us to make a direct comparison of the magnitude of the effect. It should be noted that the chirality of the crystal structure in the two experiments was determined by different methods. In Ref.[11], the chirality was determined by modern scanning transmission electron microscopy (STEM) technique[42, 43], while in Ref.[41] it was determined by the more traditional method of the etch pits[44]. It is known that determination of chirality of trigonal tellurium is a non-trivial task, and the results of different methods are not always consistent (see appendix B of [45] for a systematic analysis). On the theoretical part, another article appeared recently [46] showing that with a different choice of the collision integral (beyond the constant relaxation time approximation), the sign of the eMChA conductivity can be changed.

Summary. In this letter, we derived equations for quantifying eMChA in real materials using the Boltzmann-transport formalism within the constant relaxation time approximation. We use p-Te as a research platform and employ DFT and Wannier interpolation to make theoretical predictions for eMChA conductivity σ_{abcd} and measurable tensor γ'_{abcd} . We find that with low acceptor concentrations, the orbital Zeeman coupling is the primary origin of the eMChA response compared with spin Zeeman coupling and Berry curvature contributions. We cannot boast of an excellent agreement with experimental data, but neither do we find consistency between different experiments. Therefore, we hope that our results will be a good reference and motivation for further experimental and theoretical investigations. The developed methodology is made available via an opensource code in order to motivate further first-principles investigations of other materials.

X.L. acknowledges financial support from the China Scholarship Council and from the National Key R&D Program of China (Grant No. 2022YFA1403700). S.S.T. was funded by the European Union [H2020-MSCA-COFUND-2020-101034228-WOLFRAM2]. work of I.S and S.S.T was funded by MCIN MCIN/AEI/10.13039/501100011033 through Grant No. PID2021-129035NB-I00, and by the European Union NextGenerationEU/PRTR-C17.I1, as well as by the IKUR Strategy under the collaboration agreement between the Donostia International Physics Center and the Materials Physics Center on behalf of the Department of Education of the Basque Government. The numerical calculations were supported by Center for Computational Science and Engineering of SUSTech. We would like to thank G. L. J. A Rikken for useful discussions.

- [1] C. M. Hurd, <u>The Hall effect in metals and alloys</u> (Plenum, 1972).
- [2] A. B. Pippard, <u>Magnetoresistance in metals</u>, Vol. 2 (Cambridge university press, 1989).
- [3] E. Deyo, L. Golub, E. Ivchenko, and B. Spivak, Semiclassical theory of the photogalvanic effect in non-centrosymmetric systems, arXiv preprint 10.48550/arXiv.0904.1917 (2009).
- [4] I. Sodemann and L. Fu, Quantum nonlinear hall effect induced by berry curvature dipole in time-reversal invariant materials, Phys. Rev. Lett. 115, 216806 (2015).
- [5] K. Kang, T. Li, E. Sohn, J. Shan, and K. F. Mak, Nonlinear anomalous hall effect in few-layer WTe₂, Nature materials 18, 324 (2019).
- [6] G. L. J. A. Rikken, J. Fölling, and P. Wyder, Electrical magnetochiral anisotropy, Phys. Rev. Lett. 87, 236602 (2001).
- [7] M. Atzori, C. Train, E. A. Hillard, N. Avarvari, and G. L. J. A. Rikken, Magneto-chiral anisotropy: From fundamentals to perspectives, Chirality 33, 844 (2021).
- [8] T. Ideue, K. Hamamotol, S. Koshikawal, M. Ezawa, S. Shimizu, Y. Kaneko, Y. Tokura, N. Nagaosa, and Y. Iwasa, Bulk rectification effect in a polar semiconductor, Nature Phys. 13, 578 (2017).
- [9] R. Yoshimi, M. Kawamura, K. Yasuda, A. Tsukazaki, K. S. Takahashi, M. Kawasaki, and Y. Tokura, Nonreciprocal electrical transport in the multiferroic semiconductor (ge,mn)te, Phys. Rev. B 106, 115202 (2022).
- [10] Y. Tokura and N. Nagaosa, Nonreciprocal responses from non-centrosymmetric quantum materials, Nat. Commun. 9, 3740 (2018).
- [11] F. Calavalle, M. Suárez-Rodríguez, B. Martín-García, A. Johansson, D. C. Vaz, H. Yang, I. V. Maznichenko, S. Ostanin, A. Mateo-Alonso, A. Chuvilin, et al., Gatetuneable and chirality-dependent charge-to-spin conversion in tellurium nanowires, Nature Materials 21, 526 (2022).
- [12] V. Krstić, S. Roth, M. Burghard, K. Kern, and G. L. J. A. Rikken, Magneto-chiral anisotropy in charge transport through single-walled carbon nanotubes, J. Chem. Phys. 117, 11315 (2002).
- [13] F. Pop, P. Auban-Senzier, E. Canadell, G. L. Rikken, and N. Avarvari, Electrical magnetochiral anisotropy in a bulk chiral molecular conductor, Nature Communications 5, 1 (2014).
- [14] T. Yokouchi, Y. Ikeda, T. Morimoto, and Y. Shiomi, Giant magnetochiral anisotropy in weyl semimetal wte₂ induced by diverging berry curvature, Phys. Rev. Lett. 130, 136301 (2023).
- [15] G. L. J. A. Rikken and N. Avarvari, Strong electrical magnetochiral anisotropy in tellurium, Phys. Rev. B 99, 245153 (2019).
- [16] D. Hirobe, Y. Nabei, and H. M. Yamamoto, Chirality-induced intrinsic charge rectification in a tellurium-based field-effect transistor, Phys. Rev. B 106, L220403 (2022).
- [17] C. Niu, G. Qiu, Y. Wang, P. Tan, M. Wang, J. Jian, H. Wang, W. Wu, and P. D. Ye, Tunable chiralitydependent nonlinear electrical responses in 2d tellurium, Nano letters 23, 8445 (2023).
- [18] C. Baumgartner, L. Fuchs, A. Costa, S. Reinhardt, S. Gronin, G. C. Gardner, T. Lindemann, M. J. Manfra,

- P. E. Faria Junior, D. Kochan, <u>et al.</u>, Supercurrent rectification and magnetochiral effects in symmetric josephson junctions, Nature nanotechnology **17**, 39 (2022).
- [19] B. Pal, A. Chakraborty, P. K. Sivakumar, M. Davydova, A. K. Gopi, A. K. Pandeya, J. A. Krieger, Y. Zhang, M. Date, S. Ju, et al., Josephson diode effect from cooper pair momentum in a topological semimetal, Nature physics 18, 1228 (2022).
- [20] R. Wakatsuki, Y. Saito, S. Hoshino, Y. M. Itahashi, T. Ideue, M. Ezawa, Y. Iwasa, and N. Nagaosa, Nonreciprocal charge transport in noncentrosymmetric superconductors, Science Advances 3, e1602390 (2017).
- [21] F. Ando, Y. Miyasaka, T. Li, J. Ishizuka, T. Arakawa, Y. Shiota, T. Moriyama, Y. Yanase, and T. Ono, Observation of superconducting diode effect, Nature 584, 373 (2020).
- [22] L. Bauriedl, C. Bäuml, L. Fuchs, C. Baumgartner, N. Paulik, J. M. Bauer, K.-Q. Lin, J. M. Lupton, T. Taniguchi, K. Watanabe, et al., Supercurrent diode effect and magnetochiral anisotropy in few-layer nbse2, Nature communications 13, 4266 (2022).
- [23] D. Xiao, M.-C. Chang, and Q. Niu, Berry phase effects on electronic properties, Rev. Mod. Phys. 82, 1959 (2010).
- [24] Y. Gao, Semiclassical dynamics and nonlinear charge current, Front. Phys. 14, 33404 (2019).
- [25] Y. Gao, S. A. Yang, and Q. Niu, Intrinsic relative magnetoconductivity of nonmagnetic metals, Phys. Rev. B 95, 165135 (2017).
- [26] See supplemental material.
- [27] Y. Gao, S. A. Yang, and Q. Niu, Field induced positional shift of bloch electrons and its dynamical implications, Phys. Rev. Lett. 112, 166601 (2014).
- [28] J. Paier, M. Marsman, K. Hummer, G. Kresse, I. C. Gerber, and J. G. Ángyán, Screened hybrid density functionals applied to solids, J. Chem. Phys. 124, 154709 (2006).
- [29] G. Kresse and D. Joubert, From ultrasoft pseudopotentials to the projector augmented-wave method, Phys. Rev. B 59, 1758 (1999).
- [30] G. Kresse and J. Furthmüller, Efficiency of ab-initio total energy calculations for metals and semiconductors using a plane-wave basis set, Computational materials science 6, 15 (1996).
- [31] G. Kresse and J. Furthmüller, Efficient iterative schemes for ab initio total-energy calculations using a plane-wave basis set, Phys. Rev. B 54, 11169 (1996).
- [32] X. Wang, J. R. Yates, I. Souza, and D. Vanderbilt, Ab initio calculation of the anomalous Hall conductivity by Wannier interpolation, Phys. Rev. B 74, 195118 (2006).
- [33] G. Pizzi, V. Vitale, R. Arita, S. Blügel, F. Freimuth, G. Géranton, M. Gibertini, D. Gresch, C. Johnson, T. Koretsune, J. Ibañez-Azpiroz, H. Lee, J.-M. Lihm, D. Marchand, A. Marrazzo, Y. Mokrousov, J. I. Mustafa, Y. Nohara, Y. Nomura, L. Paulatto, S. Poncé, T. Ponweiser, J. Qiao, F. Thöle, S. S. Tsirkin, M. Wierzbowska, N. Marzari, D. Vanderbilt, I. Souza, A. A. Mostofi, and J. R. Yates, Wannier90 as a community code: new features and applications, Journal of Physics: Condensed Matter 32, 165902 (2020).
- [34] S. S. Tsirkin, High performance wannier interpolation of berry curvature and related quantities with wannierberri code, npj Computational Materials 7, 1 (2021).
- [35] X. Liu, S. S. Tsirkin, and I. Souza, Covariant derivatives of berry-type quantities: Application to nonlinear trans-

- port, arXiv preprint, 2303.10129 (2023).
- [36] O. Jepson and O. Anderson, The electronic structure of hcp ytterbium, Solid State Communications 9, 1763 (1971).
- [37] M. Methfessel and A. T. Paxton, High-precision sampling for brillouin-zone integration in metals, Phys. Rev. B 40, 3616 (1989).
- [38] S. V. Gallego, J. Etxebarria, L. Elcoro, E. S. Tasci, and J. M. Perez-Mato, Automatic calculation of symmetryadapted tensors in magnetic and non-magnetic materials: a new tool of the Bilbao Crystallographic Server, Acta Crystallographica Section A 75, 438 (2019).
- [39] The MTENSOR code package is available at the Bilbao Crystallographic Server https://www.cryst.ehu.es/cgi-bin/cryst/programs/mtensor.pl.
- [40] S. S. Tsirkin, P. A. Puente, and I. Souza, Gyrotropic effects in trigonal tellurium studied from first principles, Phys. Rev. B 97, 035158 (2018).
- [41] S. Okumura, R. Tanaka, and D. Hirobe, Chiral orbital

- texture in nonlinear electrical conduction, Phys. Rev. B 110, L020407 (2024).
- [42] Z. Dong and Y. Ma, Atomic-level handedness determination of chiral crystals using aberration-corrected scanning transmission electron microscopy, Nature Communications 11, 1588 (2020).
- [43] A. Ben-Moshe, A. Da Silva, A. Müller, A. Abu-Odeh, P. Harrison, J. Waelder, F. Niroui, C. Ophus, A. M. Minor, M. Asta, et al., The chain of chirality transfer in tellurium nanocrystals, Science 372, 729 (2021).
- [44] A. Koma and S. Tanaka, Etch pits and crystal structure of tellurium, physica status solidi (b) 40, 239 (1970).
- [45] T. Furukawa, Y. Watanabe, N. Ogasawara, K. Kobayashi, and T. Itou, Current-induced magnetization caused by crystal chirality in nonmagnetic elemental tellurium, Phys. Rev. Res. 3, 023111 (2021).
- [46] L. E. Golub, E. L. Ivchenko, and B. Spivak, Semiclassical theory of the circular photogalvanic effect in gyrotropic systems, Phys. Rev. B 102, 085202 (2020).